NASA/TM–20220002081

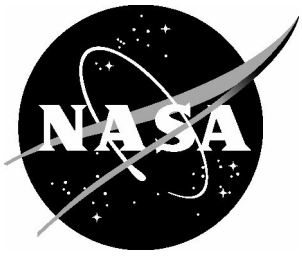

A Cohesive Element Formulation for Simulation of General Mode I, II, and III Delamination

N. V. De Carvalho and J. G. Ratcliffe
Langley Research Center, Hampton, Virginia

February 2022

NASA STI Program Report Series

Since its founding, NASA has been dedicated to the advancement of aeronautics and space science. The NASA scientific and technical information (STI) program plays a key part in helping NASA maintain this important role.

The NASA STI program operates under the auspices of the Agency Chief Information Officer. It collects, organizes, provides for archiving, and disseminates NASA's STI. The NASA STI program provides access to the NTRS Registered and its public interface, the NASA Technical Reports Server, thus providing one of the largest collections of aeronautical and space science STI in the world. Results are published in both non-NASA channels and by NASA in the NASA STI Report Series, which includes the following report types:

- TECHNICAL PUBLICATION. Reports of completed research or a major significant phase of research that present the results of NASA Programs and include extensive data or theoretical analysis. Includes compilations of significant scientific and technical data and information deemed to be of continuing reference value. NASA counterpart of peer-reviewed formal professional papers but has less stringent limitations on manuscript length and extent of graphic presentations.

- TECHNICAL MEMORANDUM. Scientific and technical findings that are preliminary or of specialized interest, e.g., quick release reports, working papers, and bibliographies that contain minimal annotation. Does not contain extensive analysis.

- CONTRACTOR REPORT. Scientific and technical findings by NASA-sponsored contractors and grantees.

- CONFERENCE PUBLICATION. Collected papers from scientific and technical conferences, symposia, seminars, or other meetings sponsored or co-sponsored by NASA.

- SPECIAL PUBLICATION. Scientific, technical, or historical information from NASA programs, projects, and missions, often concerned with subjects having substantial public interest.

- TECHNICAL TRANSLATION. English-language translations of foreign scientific and technical material pertinent to NASA's mission.

Specialized services also include organizing and publishing research results, distributing specialized research announcements and feeds, providing information desk and personal search support, and enabling data exchange services.

For more information about the NASA STI program, see the following:

- Access the NASA STI program home page at http://www.sti.nasa.gov

- Help desk contact information:

https://www.sti.nasa.gov/sti-contact-form/
and select the "General" help request type.

NASA/TM–20220002081

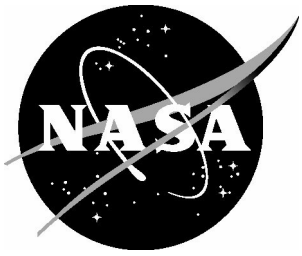

A Cohesive Element Formulation for Simulation of General Mode I, II, and III Delamination

N. V. De Carvalho and J. G. Ratcliffe
Langley Research Center, Hampton, Virginia

National Aeronautics and
Space Administration

Langley Research Center
Hampton, Virginia 23681-2199

February 2022

Available from:

NASA STI Program / Mail Stop 148
NASA Langley Research Center
Hampton, VA 23681-2199
Fax: 757-864-6500

Abstract

Cohesive element formulations proposed for simulating mixed-mode delamination in laminated composites assume that Mode II and Mode III fracture processes, and hence traction-separation laws, are identical. However, experimental observations suggest that such an assumption may not hold in general. The approach described herein consists of a cohesive element formulation in which the assumption of identical Mode II and Mode III fracture processes is not required. This assumption is alleviated by estimating the normal to the delamination front based on the gradient of the displacement jumps determined within each element. The estimated normal is used to rotate the cohesive element coordinate system. Determining the displacement jumps in the rotated coordinate system enables the distinction between Mode II sliding, and Mode III tearing. This information is subsequently used to extend a recently proposed cohesive formulation, resulting in an approach that can simulate mixed-mode I/II/III fracture via prescribing piecewise-linear traction-separation laws combined with a 3D mixed-mode fracture criteria.

1 Introduction

Several cohesive element formulations for simulating mixed-mode delamination in laminated composites have been proposed, however, these formulations do not consider Mode II and Mode III critical energy release rates to be distinct, e.g. [1–6]. However, experimental evidence suggests that Mode III loading leads to a distinct fracture process compared to Mode II loading and hence different critical Energy Release Rates (ERR), similar to what is observed between Mode I and Mode II fracture, e.g. [7]. In the case of tape-based composites, recent work indicates that delaminations under predominantly Mode III loading conditions may be difficult to grow in practice [8, 9]. Evidence of delamination migration arising from intralaminar cracking in Edge Crack Torsion (ECT) specimens that have been proposed for measuring Mode III critical ERR highlighted this difficulty [10]. Under Mode III loading, local Mode I echelon micro-cracks develop, accumulate, and lead to delamination migration unless both bounding plies are oriented to enable their containment [8]. However, containment conditions seem difficult to enforce in general [9], and hence may not occur often in practice in tape-based composites. On the other hand, preliminary work with 2D woven laminates suggests that Mode III delamination may grow and be contained, and that the associated Mode III critical ERR is distinct from the Mode II critical ERR [7, 11]. Hence, an accurate and general delamination growth simulation approach should aim to capture the potential differences between Mode I, II and III fracture processes and associated critical ERRs.

Recently a cohesive element formulation has been proposed that enables distinct piecewise-linear Traction-Separation Laws (TSLs) to be prescribed for Mode I and shear loadings, hence assuming that the Mode II and III fracture processes are identical [12]. The prescribed TSLs are followed exactly if the loading modes are pure Mode I or pure shear. Under mixed-mode loading conditions, the pure mode TSLs are scaled such that the energy dissipated equals the critical ERR determined by the selected mixed-mode fracture criterion. In addition, the scaling procedure is defined such that it ensures that the formulation satisfies the thermodynamic consistency condition proposed in [5].

In the present work, the formulation proposed in [12] is extended to enable distinct piecewise linear TSLs to be prescribed for pure Mode I, II and III loading. The distinction between Mode II and III contributions to the fracture process is performed in three steps. First the normal to the delamination front is estimated based on the gradient of the magnitude of the displacement jump. Subsequently, the cohesive element local coordinate system is rotated such that one of the components is aligned with the normal to the delamination front. Finally, the components of the displacement jump are computed in the new coordinate system, with Mode II sliding shear given by the component of the displacement jump determined along the direction normal to the delamination front, and Mode III tearing shear associated with the component of the displacement jump determined along the delamination front. The simulation of general mixed-mode I/II/III is enabled by adopting the 3D mixed-mode fracture criterion proposed in [13] . The fracture criterion in [13] provides a general expression for the critical ERR as a function of the Mode I, II and III critical ERRs and the Mode II and III mode-mixities.

In what follows, a summary of the cohesive element formulation is presented, highlighting the key steps taken to extend the formulation proposed in [12]. In Section 3, results from the verification exercises performed are reported, providing a preliminary assessment of the accuracy of the approach when used to simulate Mode I, II, III and mixed-mode I/II/III delamination growth. Finally, a summary of the key findings is presented in Section 4.

2 Cohesive Formulation

This section details how the formulation proposed in [12] can be extended to enable the simulation of general mixed-mode I/II/III fracture in which the fracture processes associated with Mode II and Mode III loading may be distinct. In Section 2.1 the procedure used to estimate the normal to the delamination front and distinguish between Mode II sliding and Mode III tearing is provided. In section 2.2 the calculation of the displacement jumps associated with Mode II and Mode III is illustrated. An overview of the piecewise-linear TSL definition adopted in [12] is provided in Section 2.3 for completeness. Subsequently, the treatment of mixed-mode conditions discussed in [12] is extended to account for the distinction between Mode II and Mode III contributions to the fracture process. This distinction also requires revisiting the fracture criterion used [12] and adopting a 3D fracture criterion, Section 2.5. Finally, the expression for the secant stiffness is provided in Section 2.6.

2.1 Calculating a normal to the delamination front

In the present work, the normal to the delamination front, in the element coordinate system, is assumed to be well estimated by:

$$\mathbf{n}_{ce} = -\left(\frac{\partial \delta_T}{\partial x_{ce}}, \frac{\partial \delta_T}{\partial y_{ce}}, 0\right) \tag{1}$$

where δ_T designates the magnitude of the displacement jump and $\left(\frac{\partial}{\partial x_{ce}}, \frac{\partial}{\partial y_{ce}}\right)$ are the spatial derivatives in the cohesive element coordinate system. The negative sign reflects

the fact that the magnitude of the displacement jump tends towards zero approaching the delamination front, and hence the gradient of the displacement jump is oriented towards the delamination wake and not the front.

The procedure used to evaluate Eq. 1 is detailed next. Consider a transformation matrix relating the global coordinate system to the element coordinate system:

$$\mathbf{x}_{ce} = \mathbf{T}\mathbf{x}_g \tag{2}$$

The matrix $\mathbf{T}$ can be trivially obtained following [14]. The displacement jump vector $\boldsymbol{\delta}^i$ between a node on the top surface i^+ and a corresponding node i^- on the bottom surface of the cohesive element, can be obtained by:

$$\boldsymbol{\delta}^i = \mathbf{T}(\mathbf{u}^{i^+} - \mathbf{u}^{i^-}) \tag{3}$$

in which $\boldsymbol{\delta}^i = \{\delta_{s1}, \delta_{s2}, \delta_I\}^i$. The components δ_{s1} and δ_{s2} designate shear displacement jumps and δ_I the displacement jump associated with Mode I (opening mode). The magnitude of a displacement jump is determined by:

$$\delta_T \quad = \quad \sqrt{(\delta_{s1})^2 + (\delta_{s2})^2 + (\langle\delta_I\rangle)^2} \tag{4}$$

in which the Macaulay bracket in Eq. 4 is defined as $\langle x\rangle = x$, if $x \geq 0$ and $\langle x\rangle = 0$, if $x < 0$. The element coordinate system is used to calculate the displacement jumps. The coordinates $\mathbf{x_{ce}} = [x_{ce}, y_{ce}]^\top$, within the element, relate to the element natural coordinates via:

$$\begin{bmatrix} x_{ce} \\ y_{ce} \end{bmatrix} = \begin{bmatrix} N_1(\xi,\eta) & N_2(\xi,\eta) & \dots & N_n(\xi,\eta) \\ N_1(\xi,\eta) & N_2(\xi,\eta) & \dots & N_n(\xi,\eta) \end{bmatrix} \begin{bmatrix} x_{ce}^1 & y_{ce}^1 \\ x_{ce}^2 & y_{ce}^2 \\ \vdots & \vdots \\ x_{ce}^n & y_{ce}^n \end{bmatrix} \tag{5}$$

where $\left(x_{ce}^i, y_{ce}^i\right) = \frac{1}{2}\left(\left(x_{ce}^{+i} y_{ce}^{+i}\right) + \left(x_{ce}^{-i} y_{ce}^{-i}\right)\right)$ are average nodal positions of each node pair, defining the mid-surface of the element [14], and $N_i(\xi,\eta)$ the respective shape functions. Note that $z_{ce} = 0$, and hence will be omitted. Using the chain rule, one can relate the derivates in the natural space to the derivates in the element coordinate system by:

$$\begin{bmatrix} \frac{\partial}{\partial\xi} \\ \frac{\partial}{\partial\eta} \end{bmatrix} = \mathbf{J} \begin{bmatrix} \frac{\partial}{\partial x_{ce}} \\ \frac{\partial}{\partial y_{ce}} \end{bmatrix} \tag{6}$$

in which the matrix $\mathbf{J}$, often named Jacobian, is given by:

$$\mathbf{J} = \begin{bmatrix} \frac{\partial x_{ce}}{\partial\xi} & \frac{\partial y_{ce}}{\partial\xi} \\ \frac{\partial x_{ce}}{\partial\eta} & \frac{\partial y_{ce}}{\partial\eta} \end{bmatrix} \tag{7}$$

Given Eq. 5, the Jacobian matrix can be evaluated as:

$$\mathbf{J} = \begin{bmatrix} \frac{\partial N_1(\xi,\eta)}{\partial\xi} & \frac{\partial N_2(\xi,\eta)}{\partial\xi} & \dots & \frac{\partial N_n(\xi,\eta)}{\partial\xi} \\ \frac{\partial N_1(\xi,\eta)}{\partial\eta} & \frac{\partial N_2(\xi,\eta)}{\partial\eta} & \dots & \frac{\partial N_n(\xi,\eta)}{\partial\eta} \end{bmatrix} \begin{bmatrix} x_{ce}^1 & y_{ce}^1 \\ x_{ce}^2 & y_{ce}^2 \\ \vdots & \vdots \\ x_{ce}^n & y_{ce}^n \end{bmatrix} \tag{8}$$

and $\mathbf{J}^{-1}$ can be determined by inverting Eq. 8. Knowing $\mathbf{J}^{-1}$, the derivates $\left(\frac{\partial}{\partial x_{ce}}, \frac{\partial}{\partial y_{ce}}\right)$ in the element coordinate system can be obtained from Eq. 6:

$$\begin{bmatrix} \frac{\partial}{\partial x_{ce}} \\ \frac{\partial}{\partial y_{ce}} \end{bmatrix} = \mathbf{J}^{-1} \begin{bmatrix} \frac{\partial}{\partial \xi} \\ \frac{\partial}{\partial \eta} \end{bmatrix} \tag{9}$$

The gradient of the magnitude of the displacement jump, δ_T, can be determined by:

$$\begin{bmatrix} \frac{\partial \delta_T}{\partial x_{ce}} \\ \frac{\partial \delta_T}{\partial y_{ce}} \end{bmatrix} = \mathbf{J}^{-1} \begin{bmatrix} \frac{\partial N_1(\xi,\eta)}{\partial \xi} & \frac{\partial N_2(\xi,\eta)}{\partial \xi} & \cdots & \frac{\partial N_n(\xi,\eta)}{\partial \xi} \\ \frac{\partial N_1(\xi,\eta)}{\partial \eta} & \frac{\partial N_2(\xi,\eta)}{\partial \eta} & \cdots & \frac{\partial N_n(\xi,\eta)}{\partial \eta} \end{bmatrix} \begin{bmatrix} \delta_T^1 \\ \delta_T^2 \\ \vdots \\ \delta_T^n \end{bmatrix} \tag{10}$$

in which δ_T^i are determined at each node pair using Eq. 4. The derivates at the centroid of the element are determined by evaluating Eq. 10 at $(\xi, \eta) = (0, 0)$. Finally, having determined $\left(\frac{\partial \delta_T}{\partial x_{ce}}, \frac{\partial \delta_T}{\partial y_{ce}}\right)$, the normal to the delamination front is estimated using Eq. 1, and normalized as:

$$\hat{\mathbf{n}}_{ce} = \frac{\mathbf{n}_{ce}}{\|\mathbf{n}_{ce}\|} \tag{11}$$

Further granularity may be achieved by evaluating Eq. 10 and subsequently Eq. 1 at the integration points. Determining the normal based on single evaluation of Eq. 1 at the centroid, rather than at the integration points, is an implementation option, (supported by the smooth variation of the normal across adjacent elements reported in Sections 3.2 and 3.5.2), that can be revisited if required.

2.2 Distinguishing between Mode II sliding and Mode III tearing

To distinguish between the Mode II and Mode III fracture processes, it is necessary to calculate the displacement jumps associated with Mode II sliding, δ_{II}, and Mode III tearing, δ_{III}. Having determined the normal to the crack front $\hat{\mathbf{n}}_{ce}$, Eqs. 1 and 11, δ_{II} and δ_{III} can be determined by computing the displacement jumps in a rotated coordinate system, ce', with axes across and along the normal to delamination front. An illustration of the coordinate systems ce and ce' and $\hat{\mathbf{n}}_{ce}$ is provided in Fig. 1. The procedure used to calculate δ_{II} and δ_{III} is outlined next. A matrix $\mathbf{R}$ relating the coordinate systems ce' and ce can be determined as:

$$\mathbf{R} = \begin{bmatrix} \hat{n}_{ce_1} & \hat{n}_{ce_2} & 0 \\ \hat{n}^{\perp}_{ce_2} & \hat{n}^{\perp}_{ce_2} & 0 \\ 0 & 0 & 1 \end{bmatrix} \tag{12}$$

in which $\hat{\mathbf{n}}_{ce} = (\hat{n}_{ce_1}, \hat{n}_{ce_2})$ and $\hat{\mathbf{n}}^{\perp}_{ce} = \left(\hat{n}^{\perp}_{ce_1}, \hat{n}^{\perp}_{ce_2}\right)$ is a vector perpendicular to $\hat{\mathbf{n}}_{ce}$ obtained via a counterclockwise rotation of $\hat{\mathbf{n}}_{ce}$. Using Eq. 12 in Eq. 3, the displacement jumps in ce' are given by:

$$\boldsymbol{\delta}^i_{ce'} = \mathbf{RT}(\mathbf{u}^{i^+} - \mathbf{u}^{i^-}) \tag{13}$$

where $\boldsymbol{\delta}^i_{ce'} = \{\delta_{II}, \delta_{III}, \delta_I\}^i$.

Before a crack is formed, it is not possible to distinguish between Mode II and Mode III loading, since their definition implies the existence of a crack. This is reflected in the

proposed formulation. If the interface is pristine (no delamination) and loaded uniformly, the magnitude of the displacement gradient is zero, and the normal to the delamination front cannot be determined, Eq. 1, and hence Mode II and III contributions cannot be identified. Therefore, at this condition (zero displacement gradient), either Mode II or Mode III TSL may be used at onset. Investigating the most appropriate assumption to use at onset may be of interest, but is considered out-of-scope. The present work focuses in assessing the ability of the approach to simulate delamination growth once damage as initiated.

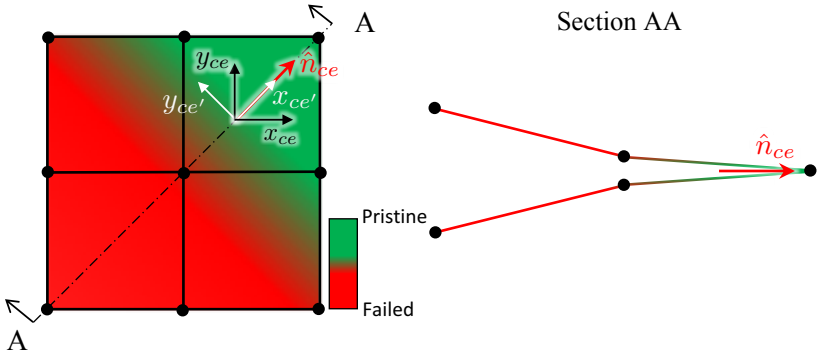

Figure 1: Illustration of coordinate systems ce and ce'. The x axis of ce' is aligned with the normal to the crack front. Coordinate system ce' is used to calculate Mode II sliding, δ_{II}, and Mode III tearing, δ_{III}.

2.3 Piecewise-linear Traction Separation Laws

Assume a piecewise-linear TSL defined by points corresponding to a change in slope in the traction-displacement relationship, $S = \{\mathbf{p}_1, ..., \mathbf{p}_m\}$, where $\mathbf{p}_1 = (\delta^{p_1}, \sigma^{p_1})$. An illustration of a piecewise-linear TSL is provided in Fig. 2. Based on [12], the critical energy release rate, G_c, for a generic piecewise-linear TSL with m number of points $\mathbf{p}_j$, ordered based on their damage state, from pristine to failed, can be determined by:

$$G_c = \frac{1}{2} \sum_{j=3}^{m} (\mathbf{p}_j \times \mathbf{p}_{j-1}) \tag{14}$$

in which it is assumed that $\mathbf{p}_1 = (0, 0)$. The first two points, $j = 1$ and $j = 2$, prescribe the interface stiffness prior to damage, and hence are not included in Eq. 14. The critical displacement jump and stress, leading to damage formation, $\delta_c(d)$, $\sigma_c(d)$, can be written as a function of a single variable $d \in [0, 1]$ using the parametric form of a 2D line for each line segment. The variable d represents damage associated with a material point. The material point is undamaged if $d = 0$ and fully damaged if $d = 1$. The value of d associated with each point $\mathbf{p}_j$ can be determined by:

$$d^{p_j} = \begin{cases} 0 & \text{if } j < 3 \\ \frac{1}{2G_c} \sum_{i=3}^{j} (\mathbf{p}_j \times \mathbf{p}_{j-1}) & \text{if } j \geq 3 \end{cases} \tag{15}$$

The critical displacement jump as a function of d is given by:

$$\delta_c(d) = \begin{cases} \delta_c^{p_2} & \text{if } d = 0 \\ \delta_c^{p_{j-1}} + \left(\delta_c^{p_j} - \delta_c^{p_{j-1}}\right) \frac{d - d^{p_{j-1}}}{d^{p_j} - d^{p_{j-1}}} & \text{if } d^{p_{j-1}} < d \leq d^{p_j} \end{cases} \tag{16}$$

for $j = 3$ to m. Similarly for $\sigma_c(d)$,

$$\sigma_c(d) = \begin{cases} \sigma^{p_2} & \text{if } d = 0 \\ \sigma^{p_{j-1}} + \left(\sigma^{p_j} - \sigma^{p_{j-1}}\right) \frac{d - d^{p_{j-1}}}{d^{p_j} - d^{p_{j-1}}} & \text{if } d^{p_{j-1}} < d \leq d^{p_j} \end{cases} \tag{17}$$

for $j = 3$ to m. The energy release rate, G, associated with an applied displacement jump, δ, along a direction corresponding to the the TSL being evaluated can be estimated by:

$$G = \frac{1}{2} \sum_{j=3}^{m} \left(\mathbf{p}_j \frac{\delta}{\delta_c\left(d\right)} \times \mathbf{p}_{j-1} \frac{\delta}{\delta_c\left(d\right)} \right) = G_c \left(\frac{\delta}{\delta_c(d)} \right)^2 \tag{18}$$

and is depicted in Fig. 2. The total energy release rate, $G_T = G_I + G_{II} + G_{III}$, can therefore be computed by:

$$G_T = G_{Ic} \left(\frac{\langle \delta_I \rangle}{\delta_{Ic}(d)} \right)^2 + G_{IIc} \left(\frac{\delta_{II}}{\delta_{IIc}\left(d\right)} \right)^2 + G_{IIIc} \left(\frac{\delta_{III}}{\delta_{IIIc}\left(d\right)} \right)^2 \tag{19}$$

in which $\delta_{Ic}(d)$, $\delta_{IIc}(d)$ and $\delta_{IIIc}(d)$ are the critical displacement jumps associated with the Mode I, Mode II and Mode III TSLs. Equation 19 extends the formulation proposed in [12] by considering separately the Mode II and III contributions.

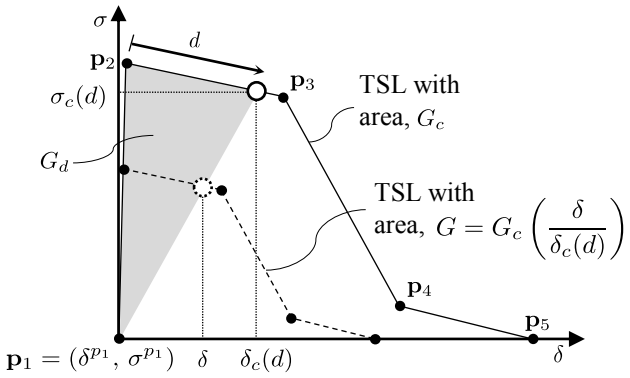

Figure 2: Ilustration of a piecewise-linear TSL.

2.4 Mixed-mode response

In the present formulation, using Eq. 18, the local Mode II and Mode III mode-mixities at each integration point are estimated by:

$$\beta_{II} = \frac{G_{II}}{G_T} = \frac{G_{IIc} \left(\frac{\delta_{II}}{\delta_{c-II}(d)} \right)^2}{G_{Ic} \left(\frac{\langle \delta_I \rangle}{(\delta_{c-I}(d))} \right)^2 + G_{IIc} \left(\frac{\delta_{II}}{\delta_{c-II}(d)} \right)^2 + G_{IIIc} \left(\frac{\delta_{III}}{\delta_{c-III}(d)} \right)^2} \tag{20}$$

$$\beta_{III} = \frac{G_{III}}{G_T} = \frac{G_{IIIc}\left(\frac{\delta_{III}}{\delta_{c-III}(d)}\right)^2}{G_{Ic}\left(\frac{\langle\delta_I\rangle}{(\delta_{c-I}(d))}\right)^2 + G_{IIc}\left(\frac{\delta_{II}}{\delta_{c-II}(d)}\right)^2 + G_{IIIc}\left(\frac{\delta_{III}}{\delta_{c-III}(d)}\right)^2} \tag{21}$$

Fracture is assumed to occur if a fracture criterion is exceeded, for example:

$$f_{cr} = \frac{G_T(d)}{G_c\left(\beta_{II}, \beta_{III}\right)} > 1 \tag{22}$$

where $G_T(d)$ is given by Eq. 19 and the expression for $G_c\left(\beta_{II}, \beta_{III}\right)$ may vary depending on the the fracture criterion chosen, see Section 2.5. For a given β_{II} and β_{III}, the TSLs associated with pure mode fracture along each loading direction, ($S_{Ic} = \{\mathbf{p}_{I_1}, ..., \mathbf{p}_{I_m}\}$, $S_{IIc} = \{\mathbf{p}_{II_1}, ..., \mathbf{p}_{II_m}\}$, and $S_{IIIc} = \{\mathbf{p}_{III_1}, ..., \mathbf{p}_{III_m}\}$) are scaled to match the critical energy release rate $G_c\left(\beta_{II}, \beta_{III}\right)$ as determined by the fracture criterion. Note that S_{Ic}, S_{IIc} and S_{IIIc} do not need to have the same shape, or be defined with the same number of points m. The scaled TSLs, as a function of the mode-mixities β_{II} and β_{III}, are designated by $S_I\left(\beta_{II},\beta_{III}\right) = \{\mathbf{p}_{I_1}\left(\beta_{II},\beta_{III}\right), ..., \mathbf{p}_{I_m}\left(\beta_{II},\beta_{III}\right)\}$, $S_{II}\left(\beta_{II},\beta_{III}\right) = \{\mathbf{p}_{II_1}\left(\beta_{II},\beta_{III}\right), ..., \mathbf{p}_{II_m}\left(\beta_{II},\beta_{III}\right)\}$ and $S_{III}\left(\beta_{II},\beta_{III}\right) = \{\mathbf{p}_{III_1}\left(\beta_{II},\beta_{III}\right), ..., \mathbf{p}_{III_m}\left(\beta_{II},\beta_{III}\right)\}$. The scaled points $\mathbf{p}_{I_i}(\beta_{II},\beta_{III})$, $\mathbf{p}_{II_i}(\beta_{II},\beta_{III})$, and $\mathbf{p}_{III_i}(\beta_{II},\beta_{III})$ associated with the correspondent TSL are given by:

$$\mathbf{p}_{I_i}\left(\beta_{II},\beta_{III}\right) = \left(\sigma_I^{p_i}\sqrt{\frac{G_c\left(\beta_{II},\beta_{III}\right)\left(1-\beta_{II}-\beta_{III}\right)}{G_{Ic}}}, \delta_I^{p_i}\sqrt{\frac{G_c\left(\beta_{II},\beta_{III}\right)\left(1-\beta_{II}-\beta_{III}\right)}{G_{Ic}}}\right) \tag{23}$$

$$\mathbf{p}_{II_i}\left(\beta_{II},\beta_{III}\right) = \left(\tau_{II}^{p_i}\sqrt{\frac{G_c\left(\beta_{II},\beta_{III}\right)\beta_{II}}{G_{IIc}}}, \delta_{II}^{p_i}\sqrt{\frac{G_c\left(\beta_{II},\beta_{III}\right)\beta_{II}}{G_{IIc}}}\right) \tag{24}$$

$$\mathbf{p}_{III_i}\left(\beta_{II},\beta_{III}\right) = \left(\tau_{III}^{p_i}\sqrt{\frac{G_c\left(\beta_{II},\beta_{III}\right)\beta_{III}}{G_{IIIc}}}, \delta_{III}^{p_i}\sqrt{\frac{G_c\left(\beta_{II},\beta_{III}\right)\beta_{III}}{G_{IIIc}}}\right) \tag{25}$$

The scaling procedure described above guarantees that a change in mode-mixity without damage being formed does not result in artificial fracture or healing, as discussed in detail in [12]. This can be assessed by noting that the ratio, $\frac{G_d}{G_c} = d$, between the energy per unit area dissipated in the fracture process G_d, depicted in Fig. 2, and the total energy per unit area required for complete fracture, G_c, is preserved if the mode-mixity changes without damage being formed, satisfying the thermodynamic consistency condition proposed in [5].

2.5 Fracture Criteria

Fracture criteria are analytical expressions that attempt to heuristically capture the variation of fracture toughness with mode-mixity, often measured experimentally in interfacial cracks. The selection of which criteria to use is guided by its ability to fit

the available experimental data [15, 16]. While other criteria could have been chosen, the present work uses the 3D mixed-mode criterion proposed in [13], which can be written as:

$$f_{cr} = \frac{G_T}{G_c\left(\beta_{II}, \beta_{III}\right)} = 1 \tag{26}$$

in which $G_c\left(\beta_{II}, \beta_{III}\right)$ is given by:

$$G_c\left(\beta_{II}, \beta_{III}\right) = G_{Ic} + \left(\left(G_{IIc} - G_{Ic}\right)\beta_{II} + \left(G_{IIIc} - G_{Ic}\right)\beta_{III}\right)\left(\beta_{II} + \beta_{III}\right)^{\eta-1} \tag{27}$$

where the constant η is determined by a best-fit to experimental data. Once fracture occurs, i.e. $f_{cr} > 1$, a new d variable is determined such that Eq. 26 is satisfied. Substituting Eq. 19 in Eq. 26, yields:

$$\frac{G_{Ic}\left(\frac{\langle\delta_I\rangle}{\delta_{c-I}(d)}\right)^2 + G_{IIc}\left(\frac{\delta_{II}}{\delta_{c-II}(d)}\right)^2 + G_{IIIc}\left(\frac{\delta_{III}}{\delta_{c-III}(d)}\right)^2}{G_c(\beta_{II}, \beta_{III})} = 1 \tag{28}$$

which results in a nonlinear equation to be solved for d. Once d is determined, to prevent artificial healing, the new damage variable d^t at a pseudo-time t is computed by:

$$d^t = \begin{cases} d & if\ d > d^{t-\Delta t} \\ d^{t-\Delta t} & if\ d \leq d^{t-\Delta t} \end{cases} \tag{29}$$

where $d^{t-\Delta t}$ is the value of d in the previous time increment.

2.6 Secant stiffness

The equation relating displacement jumps to cohesive tractions is given by:

$$\begin{bmatrix} \tau_{II} \\ \tau_{III} \\ \sigma_I \end{bmatrix} = \begin{bmatrix} K_{II}\left(d\right) & 0 & 0 \\ 0 & K_{III}\left(d\right) & 0 \\ 0 & 0 & K_I\left(d, \delta_n\right) \end{bmatrix} \begin{bmatrix} \delta_{II} \\ \delta_{III} \\ \delta_I \end{bmatrix} \tag{30}$$

where $K_{II}(d)$ and $K_{III}(d)$ are given by:

$$K_{II}\left(d\right) = \frac{\tau_{II}(d)}{\delta_{c-II}(d)} \tag{31}$$

$$K_{III}\left(d\right) = \frac{\tau_{III}(d)}{\delta_{c-III}(d)} \tag{32}$$

and $K_I\left(d, \delta_I\right)$ by:

$$K_I\left(d, \delta_I\right) = \begin{cases} \frac{\sigma_{c-I}^{p_2}}{\delta_{c-I}^{p_2}} & if\ \delta_I < 0 \\ \frac{\sigma_{c-I}(d)}{\delta_{c-I}(d)} & if\ \delta_I \geq 0 \end{cases} \tag{33}$$

The secant stiffness matrix in Eq. 30 may be fully orthotropic, i.e. $K_I(d) \neq K_{II}(d) \neq K_{III}(d)$, if the Mode I, Mode II and Mode III fracture processes, and therefore TSLs, are distinct.

The formulation proposed in the present study reduces to the one proposed in [12] if identical Mode II and III TSLs are used and the same fracture criterion is selected.

3 Finite element model analysis and results

The numerical models used and results obtained to assess and document the performance of the approach proposed are presented in the following sections. The numerical models used, including dimensions, mesh and boundary conditions, are discussed in Section 3.1.

As outlined in Section 2.2, determining the normal to the crack front is a key step to be able to determine the Mode II and Mode III contributions to the fracture process. Therefore, the verification of the approach proposed starts with an assessment of the calculation of the normal to the crack front under general conditions (evolving delamination shape), see Section 3.2. In Section 3.3 further verification results are provided, aiming to establish whether the proposed approach can simulate a Mode III fracture process that is distinct from both Mode I and II, which is the key enhancement to [12] put forward in the present work. In Section 3.4, it is assessed whether considering a Mode III fracture process that is distinct from either Mode I or Mode II compromises the accuracy with which Mode I, Mode II and mixed-mode I/II fracture is simulated. Finally the results compiled in Section 3.5 document the performance of the approach, as a function of mesh refinement and type, when used to simulate non-self-similar delamination growth under generic mixed-mode I/II/III conditions.

3.1 Finite element Models

The FE models used to assess the proposed approach were developed in Abaqus/Standard® and are illustrated in Figs. 3 to 6.

The plate model with a square delamination depicted in Fig. 3 is used to verify the procedure used to calculate the normal to the crack front. Displacement controlled loading is applied via two reference nodes, and transmitted to the nodal regions highlighted on the top and bottom surface via multi-point rigid link constraints. Symmetry boundary conditions are applied as depicted in Fig. 3 and hence only a quarter of the plate is modeled. To preserve symmetry, isotropic elastic properties were used, with Young's modulus, $E = 70000$ MPa, and Poisson's ratio, $\nu = 0.3$. The fracture process is assumed to be given by a single TSL, $S = \left\{(0.0,\, 0.0)^{p_1}\,, \left(6.0 \times 10^{-5},\, 30\right)^{p_2}\,, (1.41 \times 10^{-2},\, 0)^{p_3}\right\}$.

Numerical models of the Double Cantilever Beam (DCB), End Notch Flexure (ENF), and Mixed-Mode Bending (MMB) specimens were also developed, Fig. 4. Dimensions and boundary conditions are based on the numerical benchmarks summarized in [17]. Similar models have also been used in [12], and are repeated here to confirm that the modified approach proposed in this work preserves the accuracy demonstrated in [12], when simulating Mode I, II and mixed-mode I/II fracture. The elastic properties used and TSLs assumed in the models are given in Tables 1 and 2, respectively.

To assess the adequacy of the approach to simulate Mode III fracture, a model based on the Split Cantilever Beam (SCB) proposed in [18] was developed and is illustrated in Fig. 5. Dimensions and boundary conditions are provided in Fig. 5a. The SCB loading rig was simulated using two rod-based rigid bodies, each connected to the upper and lower arms of the specimen, as illustrated in Fig. 5b. The connections between the loading-rig and specimen are defined via displacement constraints (*Equation [21]) in Abaqus/Standard®, coupling the displacement of the rig and specimen along the y directions. The displacement constraints are established between a single node of the rig

and multiple nodes along the thickness of the arm, as highlighted in Fig. 5b. The resultant deformed shape, prior to delamination growth, is depicted in Fig. 5c. The SCB model also uses the tape-based composite elastic properties, Table 1, used when developing the DCB, MMB and ENF benchmarks. It is noted (as discussed in the introduction) that a single Mode III delamination is unlikely to propagate in unidirectional tape-based composites without accompanying matrix cracks. The tape-based properties were used for simplicity and consistency with prior work. Given the purpose of the model is to verify the accuracy of the approach, this can be done independently of the elastic properties used. The TSLs used are given in Table 2 unless otherwise specified.

The final finite element model developed in this study consists of a specimen with a pre-inserted chevron-shaped crack loaded via applied displacement along the y and z direction, as depicted in Fig. 6, imposing general mixed-mode loading conditions. For reference, the specimen is referred to as split compact tension (SCT). This model was developed to evaluate the performance of the approach in a general case of non-self-similar delamination growth under mixed-mode I/II/III loading conditions. Key aspects evaluated in this general scenario included the calculation of the normal to the crack front, and overall the mesh independence of the proposed approach. Also, in this case isotropic elastic properties were used, with Young's modulus $E = 70000$ MPa and Poisson's ratio $\nu = 0.3$. The fracture process is assumed to be described by the TSLs given in Table 2.

The formulation proposed in the present work was implemented in Abaqus/Standard® via an iso-parametric 8-noded user-defined element. Details on how to implement a cohesive formulation via an iso-parametric cohesive element can be found in [14]. A layer of zero-thickness user-defined cohesive elements, formulated as outlined in Section 2, was inserted at the center of each specimen. Native Abaqus/Standard® solid C3D8I elements were used elsewhere.

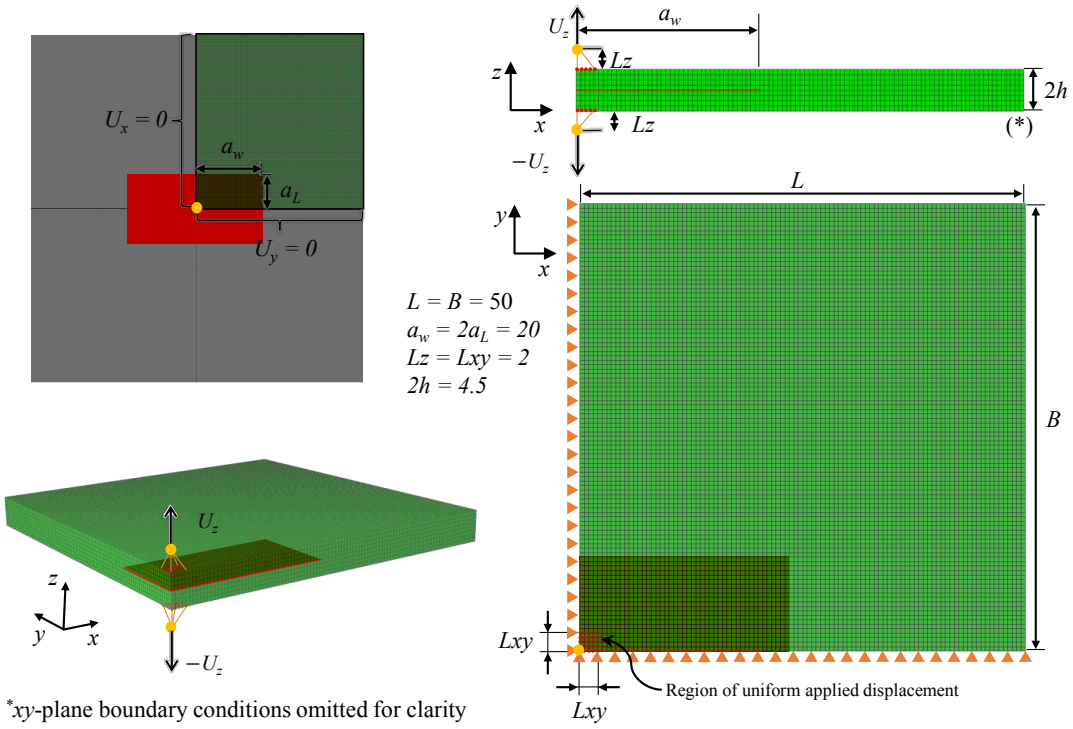

Figure 3: Plate with initial delamination $a_w \times a_L$. Quarter plate modeled using symmetry boundary conditions. Each arm was discretized with four elements through the thickness. The in-plane element size was 0.5 mm. All dimensions shown are in mm.

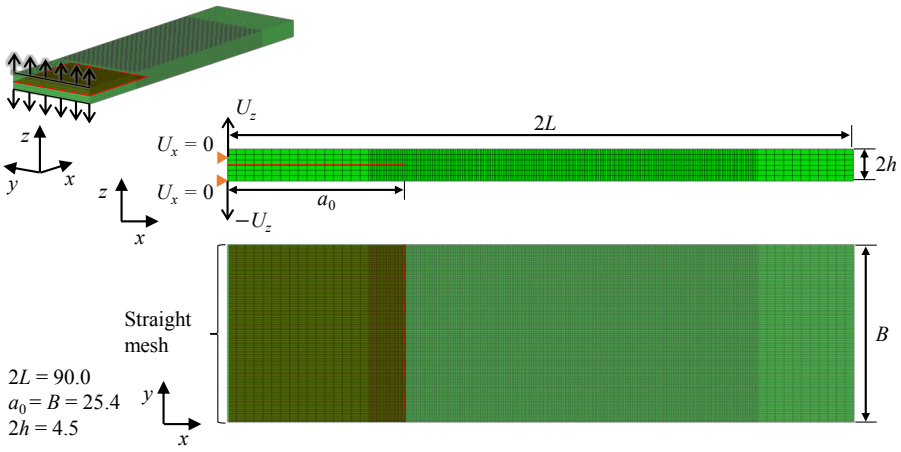

(a) Double Cantilever Beam (DCB) model.

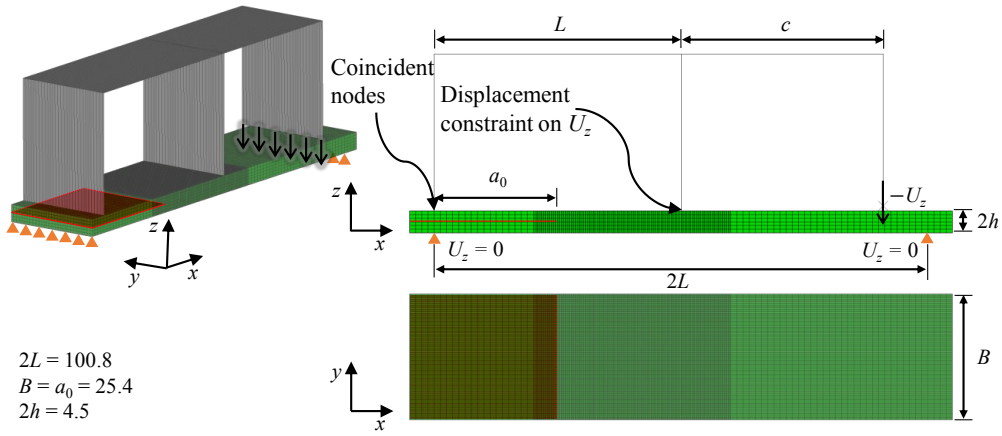

(b) Mixed-Mode Bending (MMB) model. A value of $c = 41.3$ is used to obtain the mixed-mode ratio $\beta = 0.5$ considered in this work. Rigid elements are used to represent the loading rig, following [19]. Loading rig omitted in the xy view.

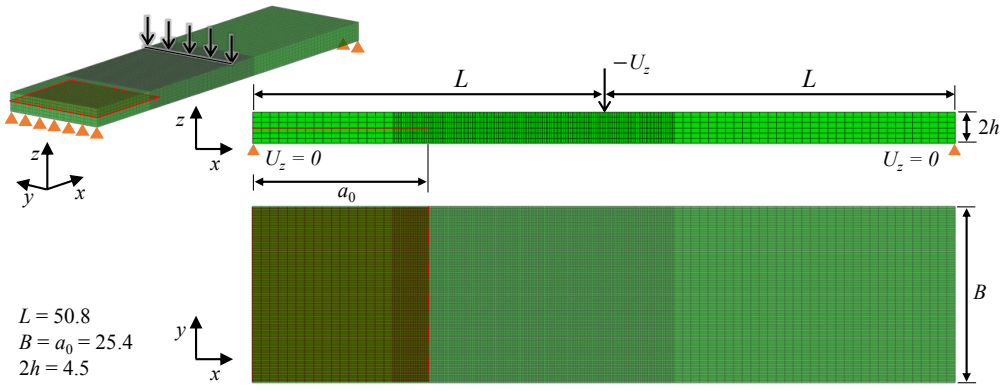

(c) End Notch Flexure (ENF) model.

Figure 4: DCB, MMB and ENF models. Dimensions, and boundary conditions based on [19]. The layup is $[0]_{24}$. Each arm was discretized with three elements through the thickness. The in-plane element size in the refined regions was 0.25 mm. All dimensions shown are in mm.

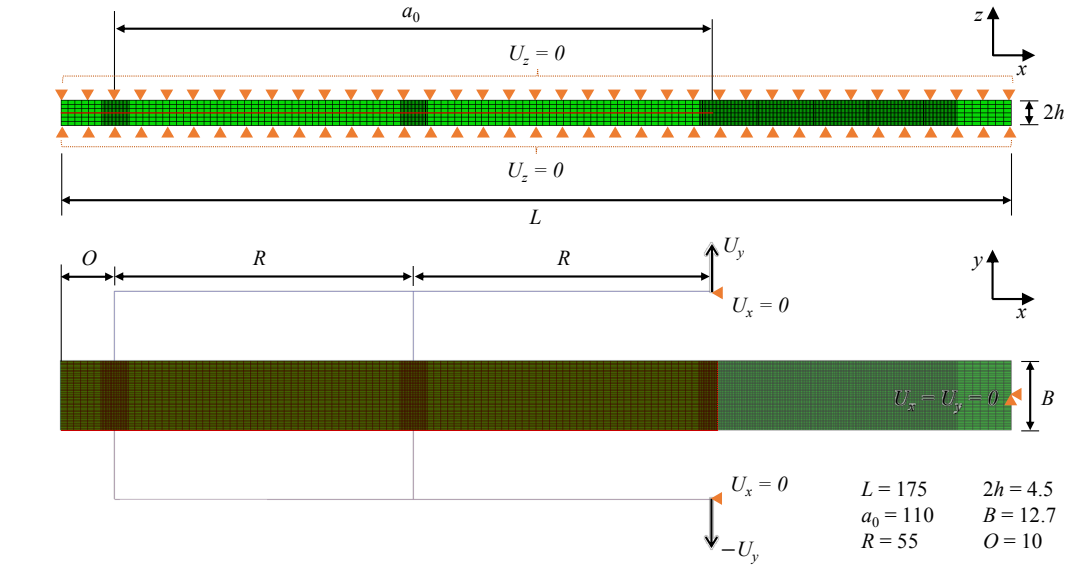

(a) Dimensions and boundary conditions.

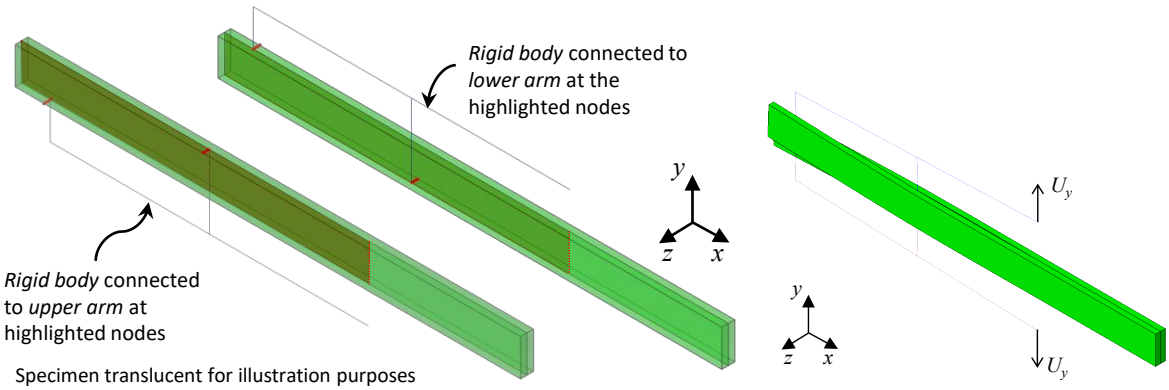

(b) Connection of rigs to the nodes of respective arms.

(c) Deformed shape.

Figure 5: Split Cantilever Beam (SCB), based on [18]. The layup is $[0]_{24}$. Each arm was discretized with three elements through the thickness. The in-plane element size in the refined regions was 0.25 mm. All dimensions shown are in mm.

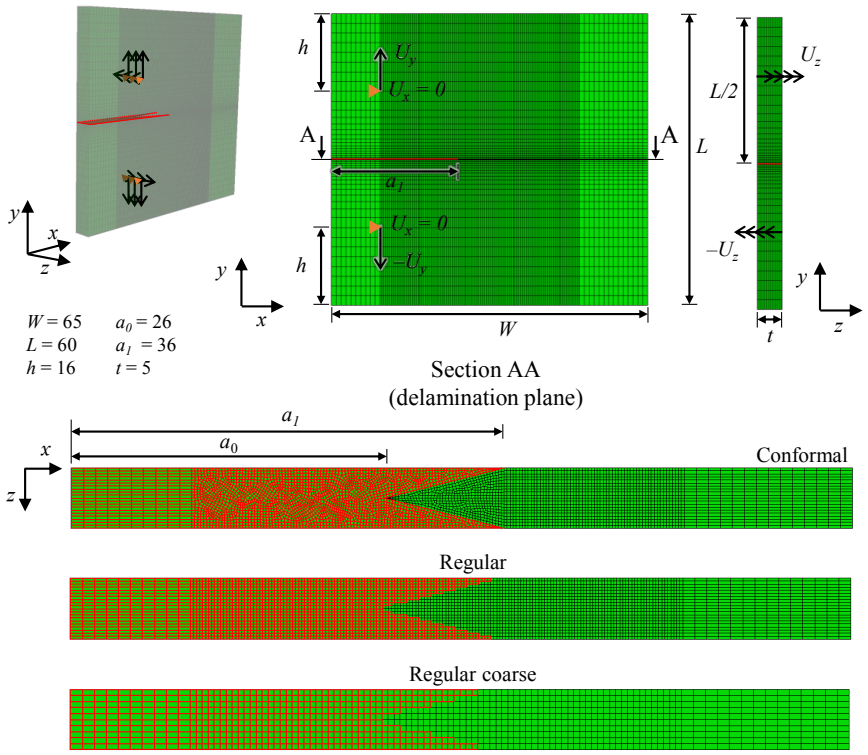

Figure 6: Split Compact Tension specimen (SCT). Three models were generated with different discretizations along the crack plane: "Conformal", "Regular" and "Regular coarse". The size of the elements within the delamination plane is approximately 0.25 mm in both the "Conformal" and "Regular" meshes, and 0.5 mm in the "Regular coarse" mesh.

Table 1: Elastic properties used in the DCB, MMB, ENF and SCB models [19, 20].

E_{11} (GPa)	$E_{22} = E_{33}$ (GPa)	$\nu_{12} = \nu_{13}$	ν_{23}	$G_{12} = G_{13}$ (GPa)	G_{23} (GPa)
161	11.38	0.32	0.44	5.17	3.98

Table 2: Mode I to III TSLs with $G_{Ic} = 0.212\,\mathrm{N/mm}$, $G_{IIc} = 0.774\,\mathrm{N/mm}$ and $G_{IIIc} = 1.548\,\mathrm{N/mm}$. Tractions given in MPa and displacement jumps in mm. First point defining the TSLs corresponds to the origin, $(0, 0)^{p_1}$. The shape of the TSLs and G_{IIIc} are assumed for illustration purposes; G_{Ic} and G_{IIc} were obtained from [19, 20]

Mode I:	$S_{Ic} = \left\{ \left(1.20 \times 10^{-4},\, 60\right)^{p_2}, \left(7.07 \times 10^{-3},\, 0\right)^{p_3} \right\}$
Mode II:	$S_{IIc} = \left\{ \left(1.20 \times 10^{-4},\, 60\right)^{p_2}, \left(2.58 \times 10^{-2},\, 0\right)^{p_3} \right\}$
Mode III:	$S_{IIIc} = \left\{ \left(1.20 \times 10^{-4},\, 60\right)^{p_2}, \left(5.16 \times 10^{-2},\, 0\right)^{p_3} \right\}$

3.2 Estimating the normal to delamination front

In Section 2.1, the procedure used to estimate the normal to the delamination front at each element is outlined. As described in Section 2.2, distinguishing between Mode II and Mode III contributions relies on the estimate of the normal to the delamination front calculated at the centroid of each element. Hence, establishing whether the procedure proposed in Section 2.1 is general and performs as intended is key to the verification of the approach proposed. The model depicted in Fig. 3 was developed to provide an assessment of the procedure used to estimate the normal to the delamination front in the general scenario of a delamination growing in a non-self-similar fashion. The initial delamination is rectangular as depicted in Fig. 3. However, given the symmetry of the geometry and loading, the delamination is expected to transition from a rectangular to a circular shape as it grows.

The delamination propagation results obtained are illustrated in Fig. 7. Figure 7 provides four snapshots of the damage state along the delamination plane taken at different solution times, as well as the normal to the delamination front calculated at each element within the process zone. The damage state is illustrated via colored dots. Each dot is located at the centroid of an element and is colored according to the value of the maximum d registered at the integration points within an element. The dot is colored red if the corresponding element has an integration point that is fully damaged, $d = 1$, and dark blue if the maximum value of d registered at any of the integration points is very small but larger than zero. Undamaged elements, with $d = 0$ at all integration points, are not depicted. Each arrow in Fig. 7 depicts the normal to the crack front calculated at the centroid of the respective element. At each solution time, the normal associated with a given element is depicted for all elements that have at least one integration point with $d > 0$ and $d < 1$. The results in Fig. 7 indicate that the orientation of the normal to the crack front is consistent with the delamination shape, suggesting the adequacy of the procedure outlined in Section 3.2. No spurious orientations are observed. For each element, the calculated normal seems to be correctly determined at onset and throughout the fracture process, changing as the delamination shape evolves. This is highlighted in Fig. 8 where the orientation associated with a single element is highlighted and plotted just after onset, Fig. 8a, and just before final failure, Fig. 8b.

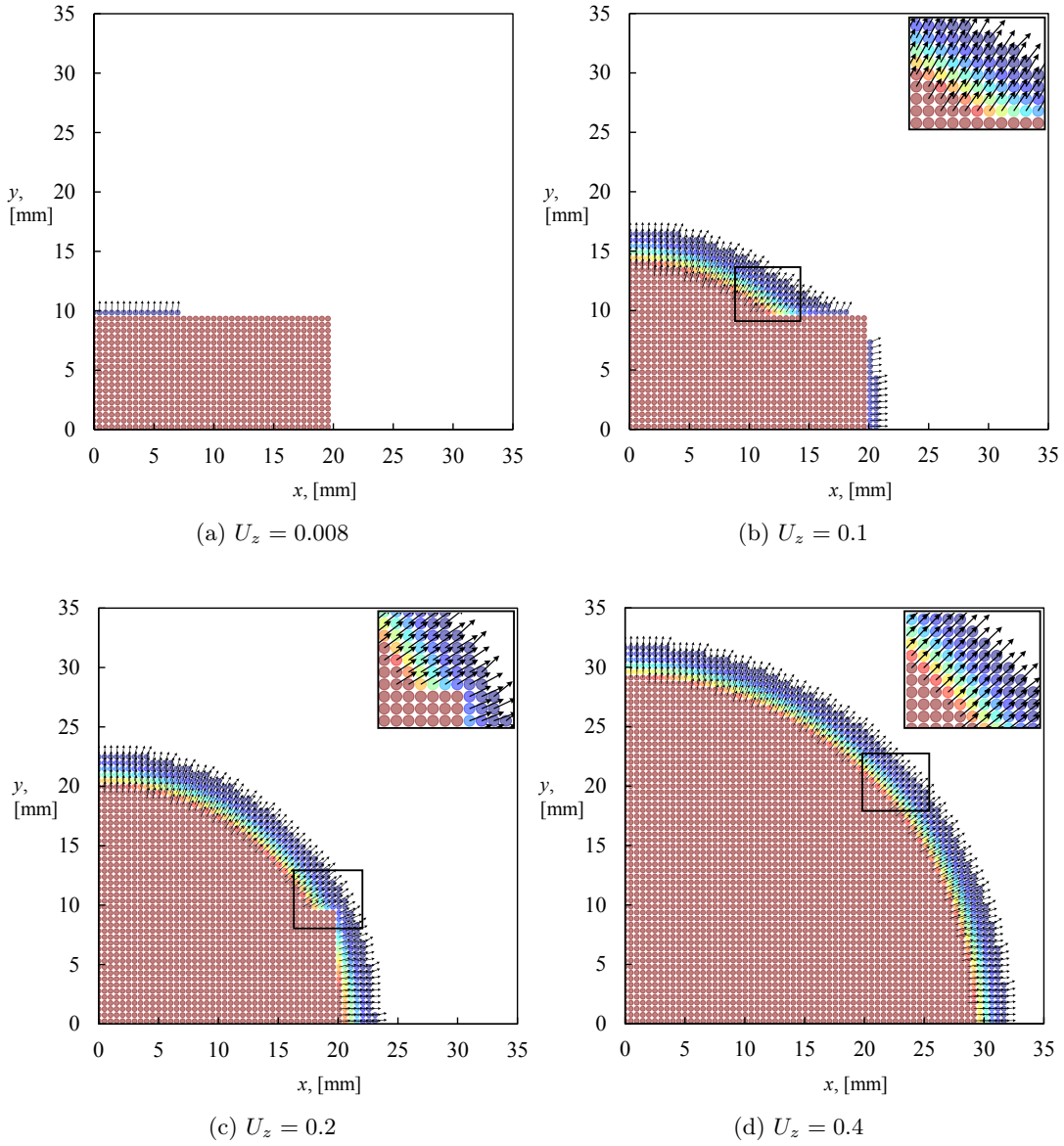

(a) $U_z = 0.008$

(b) $U_z = 0.1$

(c) $U_z = 0.2$

(d) $U_z = 0.4$

Figure 7: Delamination shape as a function of the load. Dots correspond to centroids of the elements and are colored as a function of the damage state (from red to blue). The vectors represent the normal n calculated using Eq. 1 at the centroid of each element within the process zone.

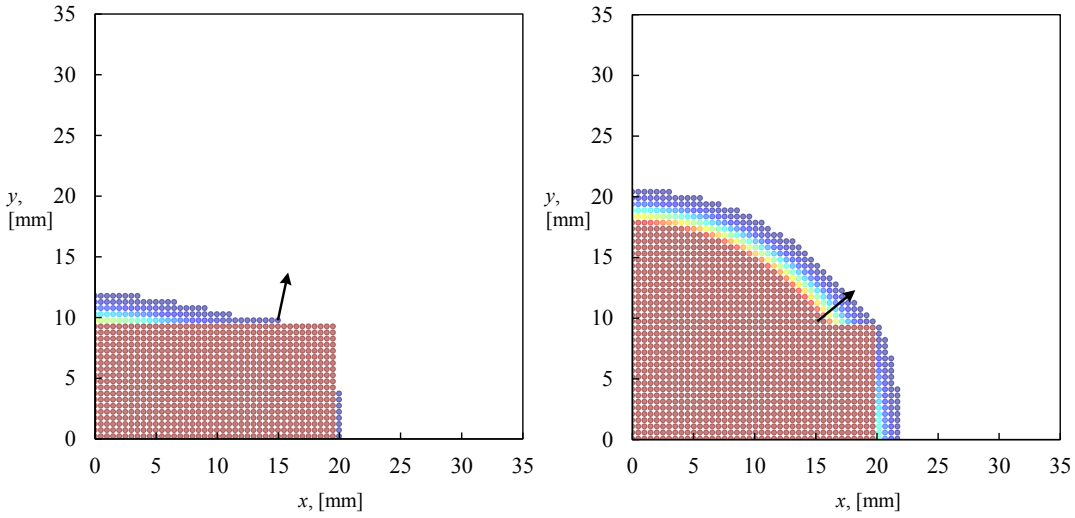

(a) $U_z = 0.044$ (b) $U_z = 0.164$

Figure 8: Normal to the delamination front calculated at onset (a) and failure (b) of an element within the process zone

3.3 Mode III fracture

To investigate whether the approach can adequately simulate Mode III fracture, the model depicted in Fig. 5 was developed, based on the Split Cantilever Beam (SCB) Mode III characterization specimen proposed in [18]. First, in Section 3.3.1 below, the Mode I to III ERRs obtained along the delamination front using the Virtual Crack Closure Technique (VCCT) are reported for reference. The results in Section 3.3.1 aim to document that the delamination front in the SCB model is loaded predominantly under Mode III conditions as intended and provide an additional quantitative reference for the results obtained with the proposed approach. Subsequently, the results obtained with the proposed approach are provided in Section 3.3.2 and compared to reference solutions to assess the adequacy of the approach to simulate Mode III fracture.

3.3.1 Mode-mixity along the delamination front - VCCT

The Virtual Crack Closure Technique (VCCT) technique, as implemented in Abaqus/Standard®, was used to determine the ERRs along the crack front of the SCB model illustrated in Fig. 5. In order to use the VCCT in Abaqus/Standard®, cohesive elements were replaced by a VCCT interface definition, following [17, 21]. The Mode I, II and III ERRs, corresponding to an applied displacement $U_y = 1\,\text{mm}$, are shown in Fig. 9a, normalized by the maximum value of ERR determined. The Mode I component is approximately zero throughout the crack front. The Mode II component is small relative to the Mode III component, except at the specimen edges. Overall, the results in Fig. 9a indicate that the SCB delamination front is loaded predominantly under Mode III conditions as intended and agree qualitatively with the results reported in [18]. Figure 9b depicts the fracture criterion, given by Eq. 26, evaluated along the crack front, based on

the energy release rates computed using VCCT and illustrated in Fig. 9a. The dashed lines labeled "min $\overline{f_{cr_{VCCT}}}$" and "avg $\overline{f_{cr_{VCCT}}}$" correspond, respectively, to the minimum and average values of the normalized fracture criterion along the front. Assuming a linear elastic model, the average and minimum values of the fracture criterion can be used to determine correspondent critical force-displacement values. In the subsequent section, the critical force-displacement values determined based on the average and minimum values of the fracture criterion are used for reference when analyzing the results obtained with the proposed approach.

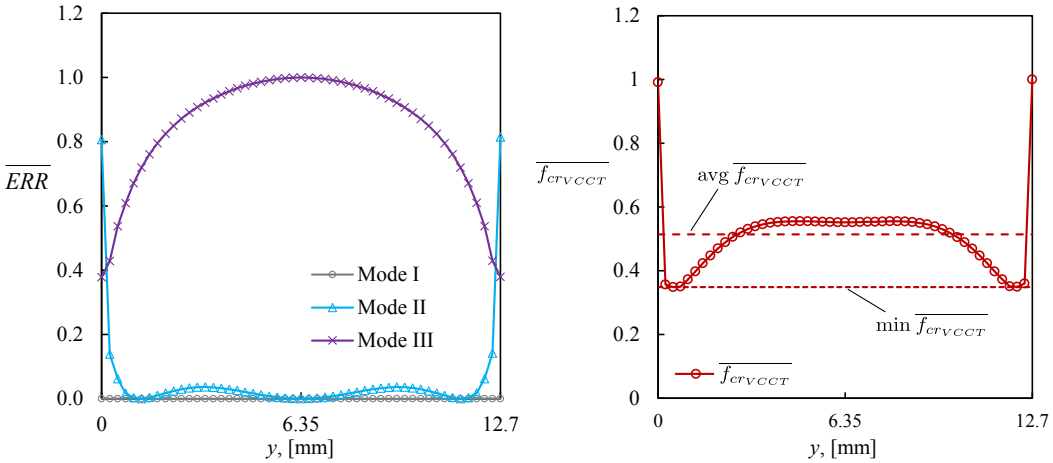

(a) Normalized ERR. (b) Normalized fracture criterion.

Figure 9: Normalized ERR and fracture criterion along the crack front of the SCB specimen.

3.3.2 Simulation of the SCB

In this section, the ability of the proposed approach to simulate a Mode III fracture process that is distinct from Mode II fracture is assessed. In the absence of a numerical benchmark, two reference simulations were obtained in which the Mode II and Mode III fracture processes were assumed to be the same. In the first simulation, labeled "$S_s = S_{II}$", the TSL used in the presence of shear loading S_s,(resulting from either Mode II or Mode III loading), was assumed to be equal to the Mode II TSL given in Table 2. This simulation provides a reference force-displacement curve for a case in which Mode III fracture is assumed to be equal to Mode II fracture. This is the typical assumption used in most cohesive element delamination simulations, and hence the expected result when using approaches that are not able to distinguish between Mode III and Mode II. As a result, these approaches assume the Mode III and Mode II fracture processes are identical; see for example [12]. In the second reference simulation, labeled "$S_s = S_{IIIc}$", the TSL used in the presence of shear loading is assumed to be equal to the Mode III TSL given in Table 2. Assuming "$S_s = S_{IIIc}$" enforces the Mode III TSL to be used in the presence of any shear loading, Mode II or Mode III. Given that the delamination in the SCB model is predominantly loaded in Mode III, the force-displacement curve obtained in the case "$S_s = S_{IIIc}$" is expected to be similar to the force displacement curve obtained with an approach that is capable of correctly reproducing the Mode III fracture process, but that does not require

assuming $S_s = S_{IIIc}$. Therefore, "$S_s = S_{IIIc}$" provides a target load-displacement curve for approaches, such as the one proposed, that aim to be able to reproduce distinct Mode III and Mode II fracture processes and hence do not assume $S_s = S_{II}$ or $S_s = S_{III}$. Finally, a simulation was performed using the TSLs given in Table 2, that represent a case in which the Mode II and Mode III fracture processes are distinct, labeled "S_{IIc}, S_{IIIc}". As can be observed in Fig. 10, the load-displacement curve obtained with the present approach is very close to the reference case $S_s = S_{IIIc}$. This indicates that the approach correctly simulates the Mode III fracture process, without needing to assume that $S_s = S_{IIIc}$. The peak force obtained is slightly smaller than the peak force obtained assuming $S_s = S_{IIIc}$, which may reflect the presence of Mode II loading and the respective critical ERR, which is lower than the Mode III critical ERR. In Figure 10 the critical force-displacements determined based on the minimum and average values of the fracture criterion calculated in the previous section are also indicated, "$F_{cr}\,(\min f_{cr_{VCCT}})$" and "$F_{cr}\,(\text{avg}\, f_{cr_{VCCT}})$", respectively. The critical force-displacement is the load required for the value of the fracture criterion to equal one. Therefore, more load is required for the minimum value of $f_{cr_{VCCT}}$ to equal one than for its average, hence "$F_{cr}\,(\min f_{cr_{VCCT}})$" is higher than "$F_{cr}\,(\text{avg}\, f_{cr_{VCCT}})$". As can be seen, the predicted maximum force-displacement agrees well with the critical force-displacement obtained using the average value of the fracture criterion. This reflects the fact that fracture criterion value along most of the crack front is very close to the average fracture criterion; see Fig. 9b.

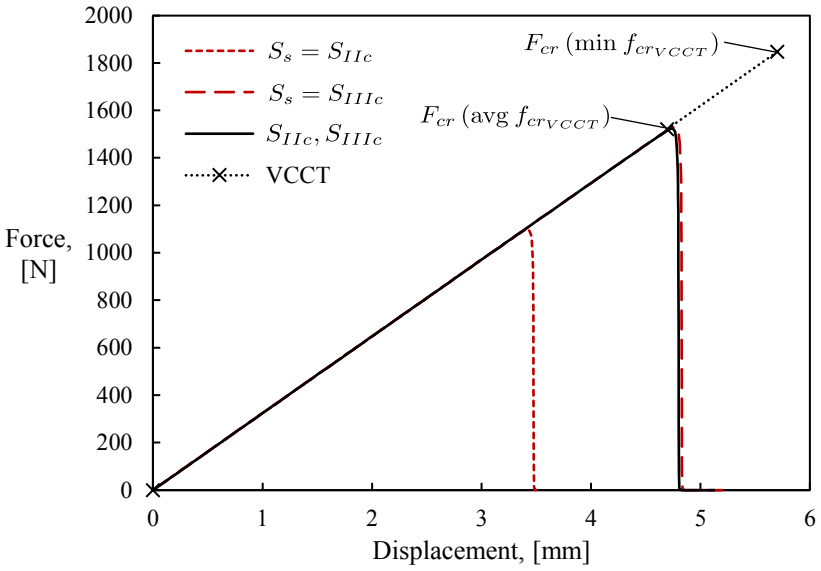

Figure 10: Force-displacement curves predicted for the SCB specimen. The curves labeled "$S_s = S_{IIc}$" and "$S_s = S_{IIIc}$" assume a single fracture process under shear loading given by the Mode II or the Mode III TSLs in Table 2, S_{IIc} and S_{IIIc}, respectively. The force-displacement curve labeled "S_{IIc}, S_{IIIc}" uses the proposed formulation and considers that the Mode II and Mode III fracture processes are distinct, and defined by S_{IIc} and S_{IIIc}, respectively. Points "$F_{cr}\,(\min f_{cr_{VCCT}})$" and "$F_{cr}\,(\text{avg}\, f_{cr_{VCCT}})$" correspond to the critical force-displacement predicted based on the minimum and average values of the fracture criterion calculated using VCCT.

3.4 Mode I, II and Mixed-Mode I/II fracture

Figures 11 to 13 compare the force-displacement curves obtained when simulating delamination growth using the models in Fig. 4 to the respective Linear Elastic Fracture Mechanics (LEFM) 2D benchmarks. For convenience, the DCB benchmark was obtained by re-deriving the benchmark reported in [22] using the elastic properties given in Table 1. The MMB and ENF benchmarks were obtained from [19, 20]. The DCB, ENF and MMB models were chosen to assess the accuracy of the approach when simulating delamination growth under Mode I, Mode II and Mixed-Mode I/II conditions, respectively, while assuming distinct Mode I, Mode II and Mode III fracture processes. The TSLs summarized in Table 2 were used in all cases. The results obtained show good agreement between the predicted load-displacement curves and the respective benchmarks. In Figs. 12 and 13, the predicted peak force is slightly lower than the benchmark. This discrepancy is attributed to the development of a non-negligible process zone prior to steady state fracture when simulating delamination growth using the cohesive approach proposed. In the LEFM benchmark, the process zone is assumed to be zero. The size of the process zone, hence the discrepancy relative to the LEFM solution, can be controlled by modifying the shape of the TSLs used [12].

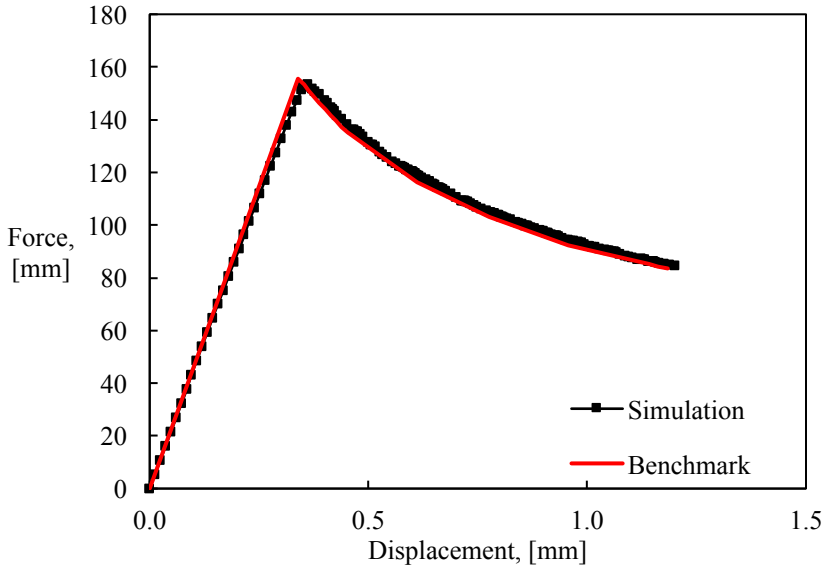

Figure 11: Double Cantilever Beam (DCB), force-displacement curve predicted with the proposed approach compared to the DCB benchmark reported in [22] re-derived using the elastic properties in Table 1.

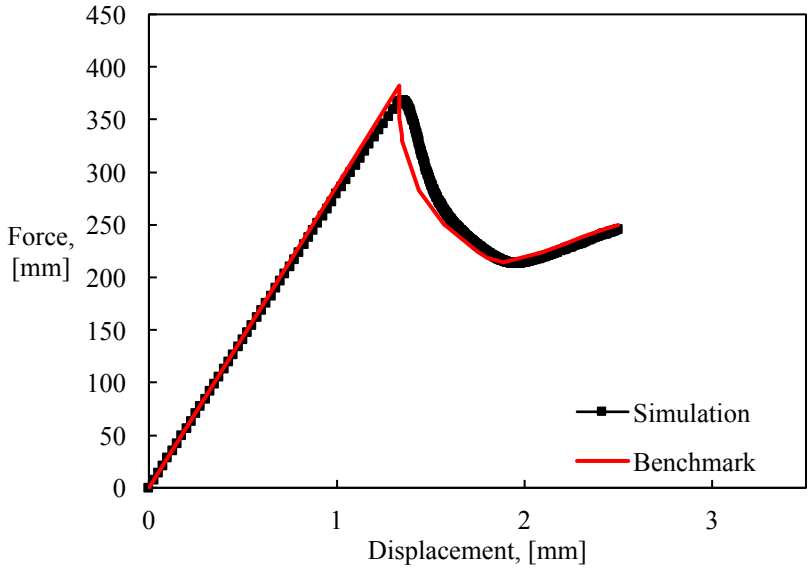

Figure 12: Mixed-Mode Bending (MMB), force-displacement curve predicted with the proposed approach compared to the MMB benchmark reported in [23].

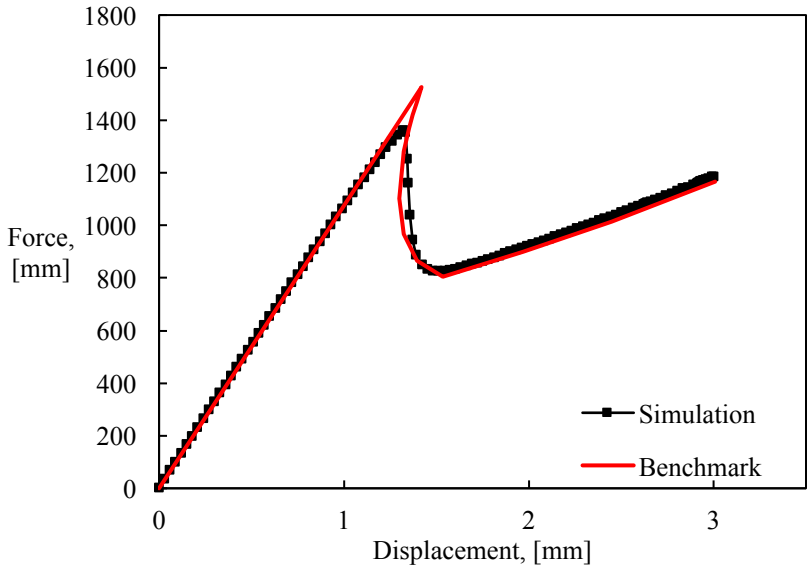

Figure 13: End Notch Flexure (ENF), force-displacement curve predicted with the proposed approach compared to the ENF benchmark reported in [20].

3.5 Mixed-Mode I, II and III fracture

In this section, the SCT model, (as illustrated in Fig. 6), is used to further generalize the assessment of the approach, focusing on studying the ability of the approach to obtain a mesh independent solution when simulating non-self-similar delamination growth under general mixed-mode conditions. The first step in this assessment was similar to

Section 3.3 where a VCCT analysis of the specimen (this time a SCT specimen) was conducted to assess the mode-mixity along a straight crack front resulting from the global loading applied, and provide an additional quantitative reference to evaluate the approach proposed. Subsequently, the results obtained from the simulation of the SCT model are reported, focusing on examining the force-displacement curves, the predicted delamination shapes, and the calculation of the normal to the delamination front at each element, as a function of mesh size, and type (structured vs. unstructured).

3.5.1 Mode-mixity along the delamination front

Similar to what was performed in Section 3.3.1, the VCCT, as implemented in Abaqus/Standard®, was used to determine the ERRs along the delamination front of the SCB model illustrated in Fig. 9. The straight delamination, with length $a_0 = a_1 = 36$ mm, was chosen to provide a reference for the steady state propagation, expected to occur once the crack evolves past the initial chevron region defined in the cohesive zone models, and illustrated in Fig. 6. The normalized components of the ERR are given in Fig. 14a. The delamination is loaded predominantly under mixed-mode I/III conditions at the center, changing to predominantly Mode II loading at the edges. The ERR components illustrated in Fig. 14a were subsequently used to evaluate the fracture criterion, Eq. 22, along the crack front. The normalized values of the fracture criterion evaluated along the crack front are reported in Fig. 14b. The dashed lines labeled "Avg $f_{cr_{VCCT}}$" and "Min $f_{cr_{VCCT}}$" correspond, respectively, to the average and minimum values of the fracture criterion along the front. Note that contrarily to what observed in Fig. 9b, the fracture criterion varies significantly along the delamination front, and is below average along most of the delamination front. The minimum and average value of the fracture criterion and their correspondent critical force-displacement values are used for reference in the following section.

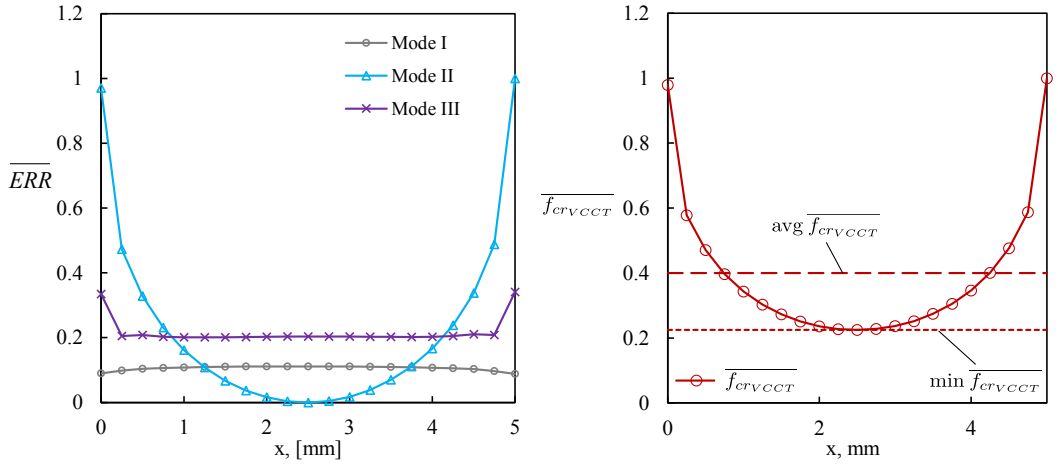

(a) Normalized ERR.

(b) Normalized fracture criterion.

Figure 14: Normalized ERR and fracture criterion along a straight crack front (i.e. $a_0 = a_1 = 36$ mm in Fig. 6) in the SCT specimen.

3.5.2 Simulation of the SCT specimen

The force-displacement curves obtained when simulating the SCT specimen are illustrated in Fig. 15. The resultant force, F_{res}, and displacement, U_{res}, are calculated as $F_{res} = \sqrt{F_y^2 + F_z^2}$ and $U_{res} = \sqrt{U_y^2 + U_z^2}$. The applied U_y and U_z relate as $\frac{U_z}{U_y} = 10$. The curves labeled "Conformal", "Regular", and "Regular Coarse" are obtained with the correspondent meshes illustrated in Fig. 6. The mapping of the chevron crack onto the regular meshes leads to an approximation of delamination shape and area. This approximation is reflected in the discrepancy between the three curves "Conformal", "Regular" and "Regular coarse", prior to delamination growth. Nevertheless, the difference between the curves is always small and the curves ultimately converge once steady state crack propagation is achieved. The dashed curve, labeled "Regular straight" was obtained by simulating the growth of a straight delamination with $a_0 = a_1 = 36\,\text{mm}$ using the approach proposed and the regular mesh depicted in Fig. 6. By choosing $a_0 = 36\,\text{mm}$, corresponding to the end of the chevron, this simulation provides a qualitative reference for the expected force-displacement curve once steady state delamination growth is obtained, and helps confirm that no spurious history dependence effects are introduced as a result of the discretization choice or due to the simulation of non-self-similar delamination growth. Furthermore, it provides a more direct comparison to the critical force-displacement points (shown as crosses along the dashed curve labeled "VCCT") determined based on the fracture criterion values calculated using VCCT, since a straight crack with $a_0 = 36\,\text{mm}$ was also assumed in the VCCT model. The peak of "Regular straight" is between the critical force-displacement calculated using VCCT based on the average fracture criterion, "$F_{cr}\,(\text{avg}\, f_{cr_{VCCT}})$", and the minimum, "$F_{cr}\,(\text{min}\, f_{cr_{VCCT}})$". This can be qualitatively explained by noting, in Fig. 14b, that the value of the fracture criterion along the crack front is not uniform, and that the average value is larger than what registered in most of the crack front.

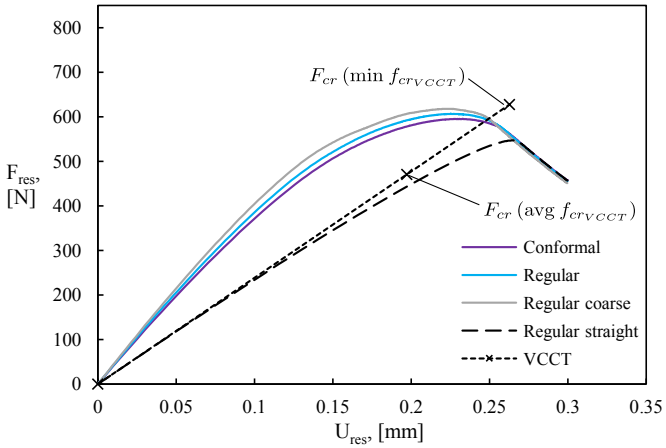

Figure 15: SCT force-displacement. Points "$F_{cr}\,(\text{min}\, f_{cr_{VCCT}})$" and "$F_{cr}\,(\text{avg}\, f_{cr_{VCCT}})$" correspond to the critical force-displacement predicted based on the minimum and average values of the fracture criterion calculated using VCCT for a straight crack with $a_0 = 36\,\text{mm}$.

In Figure 16 the crack shape as well as the normals determined at the centroid of

each element within the process zone obtained with “Conformal", “Regular” and “Regular coarse” meshes at the same applied displacements are depicted for comparison. The results obtained indicate that, as the process zone develops, Fig. 16a, the orientation of the normals as well as the shape of the process zone become similar, despite the differences in the initial crack shape and underlying mesh. As the crack progresses, Fig 16b, the differences are further attenuated, and at steady state, Fig 16c, the crack shape and normals calculated within the process zone are almost identical.

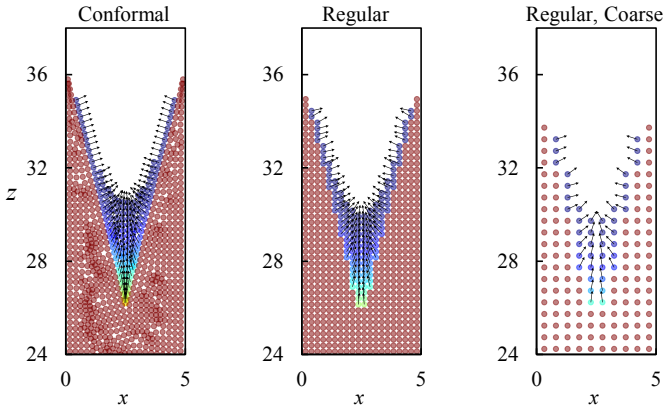

(a) $U_{res} = 0.1$

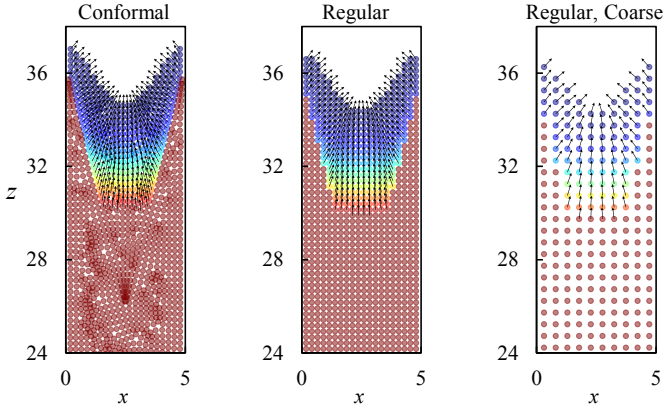

(b) $U_{res} = 0.2$

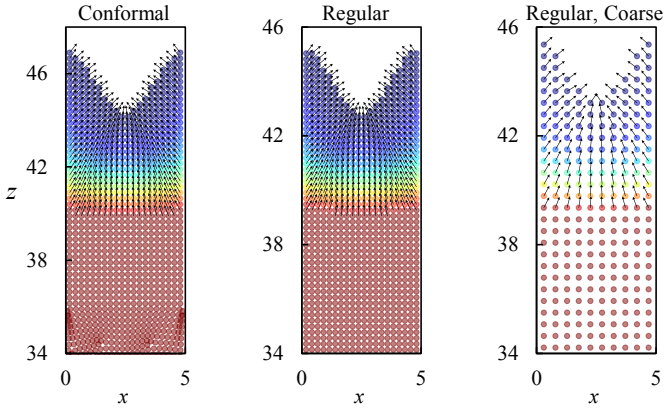

(c) $U_{res} = 0.3$

Figure 16: Delamination shape and normals to the crack front calculated at the centroid of the elements obtained with the "Conformal", "Regular" and "Regular Coarse" meshes, see Fig. 6, as a function of the applied displacement.

4 Concluding Remarks

A cohesive element formulation is proposed that can simulate delamination growth along interfaces that exhibit different Mode II and Mode III fracture processes. To distinguish between Mode II and Mode III loadings, the normal to the crack front is estimated within each element, based on the gradient of the total displacement jump. Knowing the normal to the crack front allows the partitioning of the shear displacement jump between Mode II sliding (shear displacement jump along the normal to the crack front), and Mode III tearing (shear displacement jump along the crack front). With the Mode II and Mode III displacement jumps identified, the formulation proposed in [12] is extended to enable distinct Mode II and Mode III traction separation laws to be prescribed, representing dissimilar fracture processes. In addition, a 3D mixed-mode fracture criterion is chosen to reflect the possible difference between Mode II and Mode III critical ERRs. The resultant formulation preserves all the key features of [12] such as thermodynamic consistency, and the ability to use any pure mode traction separation law shape that can be approximated via piecewise-linear function.

In the formulation proposed, determining the normal to the delamination front is key to distinguish Mode II and III fracture processes. The preliminary verification results obtained indicate that the procedure proposed to estimate the normal to the crack front provides adequate results for the general case of non-self-similar delamination growth. The subsequent verification exercises performed suggest that the approach is capable of simulating Mode I, II, mixed-mode I/II and Mode III fracture, for a case in which distinct Mode I, II and III fracture processes are assumed. Finally, the approach was applied to the general case of a delamination growing under mixed-mode I, II, III conditions in a non-self-similar fashion. The results obtained showed consistent force-displacement, crack shape and normal-to-the-crack-front calculations, for the mesh types (structured vs unstructured) and changes in mesh refinement considered. Furthermore, no spurious history effects were observed. In addition, the results were within the bounds of what would be expected based on the ERRs calculated using VCCT, assuming straight cracks, prior to growth onset.

The preliminary results obtained in this study suggest that the proposed approach is capable of correctly simulating delamination growth along an interface that exhibits distinct Mode I, II and III fracture processes. This capability eliminates the assumption that the Mode II and III fracture processes are identical, which is typically required when simulating delamination growth using cohesive element approaches.

The accuracy of the approach was demonstrated by comparison to LEFM benchmarks and reference solutions. Further work is required to generalize the accuracy assessment for fracture processes that depart from LFEM. The approach relies the characterization of pure mode TSLs and a 3D mixed-mode fracture criterion. For the approach to be applicable, these properties should adequately describe the fracture process being simulated.

In general applications, delamination may not occur in isolation and consideration of other damage modes (such as fiber kinking, fiber tensile fracture, or matrix cracks) may be required to adequately simulate damage onset and growth in composite laminates.

References

1. P. P. Camanho and C. G. Dávila. Mixed-mode decohesion finite elements for the simulation of delamination in composite materials. NASA-TM-2002-211737, National Aeronautics and Space Administration, 2002.

2. V. K. Goyal, E. R. Johnson, and C.G. Dávila. Irreversible constitutive law for modeling the delamination process using interfacial surface discontinuities. *Composite Structures*, 65(3):289 – 305, 2004.

3. W. Jiang, S. R. Hallett, B. G. Green, and M.R. Wisnom. A concise interface constitutive law for analysis of delamination and splitting in composite materials and its application to scaled notched tensile specimens. *International Journal for Numerical Methods in Engineering*, 69(9):1982–1995, 2007.

4. K. Park, G. H. Paulino, and J. R. Roesler. A unified potential-based cohesive model of mixed-mode fracture. *Journal of the Mechanics and Physics of Solids*, 57(6):891 – 908, 2009.

5. A. Turon, P. P. Camanho, J. Costa, and J. Renart. Accurate simulation of delamination growth under mixed-mode loading using cohesive elements: Definition of interlaminar strengths and elastic stiffness. *Composite Structures*, 92(8):1857 – 1864, 2010.

6. N. Nguyen and A. M. Waas. A novel mixed-mode cohesive formulation for crack growth analysis. *Composite Structures*, 156:253 – 262, 2016. 70th Anniversary of Professor J. N. Reddy.

7. N. K. Naik, K. S. Reddy, S. Meduri, N. B. Raju, P. D. Prasad, Sk. N. M. Azad, P. A. Ogde, and B. C. K. Reddy. Interlaminar fracture characterization for plain weave fabric composites. *Journal of Materials Science*, 37(14):2983–2987, 2002.

8. A. L. Horner, M. W. Czabaj, B. D. Davidson, and J. G. Ratcliffe. Three-dimensional crack surface evolution in mode III delamination toughness tests. *Engineering Fracture Mechanics*, 149:313–325, 2015.

9. C. Audd, B. D. Davidson, J. G. Ratcliffe, and M. W. Czabaj. Reexamination of the edge crack torsion test for determining the mode III delamination toughness of laminated composites. *Engineering Fracture Mechanics*, 215:138–150, 2019.

10. M.W. Czabaj, J.G. Ratcliffe, and B.D. Davidson. Observation of intralaminar cracking in the edge crack torsion specimen. *Engineering Fracture Mechanics*, 120:1–14, 2014.

11. F. A. Mehrabadi and M. Khoshravan. Mode III interlaminar fracture and damage characterization in woven fabric-reinforced glass/epoxy composite laminates. *Journal of Composite Materials*, 47(13):1583–1592, 2013.

12. N. V. De Carvalho, M. W. Czabaj, and J. G. Ratcliffe. Piecewise-linear generalizable cohesive element approach for simulating mixed-mode delamination. *Engineering Fracture Mechanics*, 242:107484, 2021.

13. J. Reeder. 3D mixed-mode delamination fracture criteria - an experimentalist's perspective. In *Proceedings of the American Society for Composites* 21^{st} *Technical Conference*, Dearborn, MI, USA, 2016.

14. V. K. Goyal. *Analytical modeling of the mechanics of nucleation and growth of cracks.* Virginia Polytechnic Institute and State University, 2002.

15. J. R. Reeder. An evaluation of mixed-mode delamination failure crieria. NASA/TM-1992-104210, National Aeronautics and Space Administration, 1992.

16. B. D. Davidson and W. Zhao. An accurate mixed-mode delamination failure criterion for laminated fibrous composites requiring limited experimental input. *Journal of Composite Materials*, 41(6):679–702, 2007.

17. R. Krueger. A summary of benchmark examples to assess the performance of quasi-static delamination propagation prediction capabilities in finite element codes. *Journal of Composite Materials*, 49(26):3297–3316, 2015.

18. F. Sharif, M. T. Kortschot, and R. H. Martin. Mode III delamination using a split cantilever beam. In *Composite Materials: Fatigue and Fracture: Fifth Volume*. ASTM International, 1995.

19. R. Krueger. Development and application of benchmark examples for mixed-mode I/II quasi-static delamination propagation predictions. NASA-CR-2012-217562, National Aeronautics and Space Administration, 2012.

20. R. Krueger. Development and application of benchmark examples for mode II static delamination propagation and fatigue growth predictions. NASA/CR-2011-217305, National Aeronautics and Space Administration, 2011.

21. DSS Simulia. *Abaqus Analysis User's Manual, Abaqus/Standard*, 6.17 edition, 2017.

22. R. Krueger. Development of a benchmark example for delamination fatigue growth prediction. NASA/CR-2010-216723, National Aeronautics and Space Administration, 2010.

23. R. Krueger and N. V. De Carvalho. In search of a time efficient approach to crack and delamination growth predictions in composites. In *Proceedings of the American Society for Composites* 31^{st} *Technical Conference*, Williamsburg, VA, USA, 2016.